Structure, Volume *24*

Supplemental Information

Structural Basis for Receptor Recognition by the Human CD59-Responsive Cholesterol-Dependent Cytolysins

Sara L. Lawrence, Michael A. Gorman, Susanne C. Feil, Terrence D. Mulhern, Michael J. Kuiper, Adam J. Ratner, Rodney K. Tweten, Craig J. Morton, and Michael W. Parker

SUPPLEMENTAL INFORMATION

SUPPLEMENTAL FIGURES

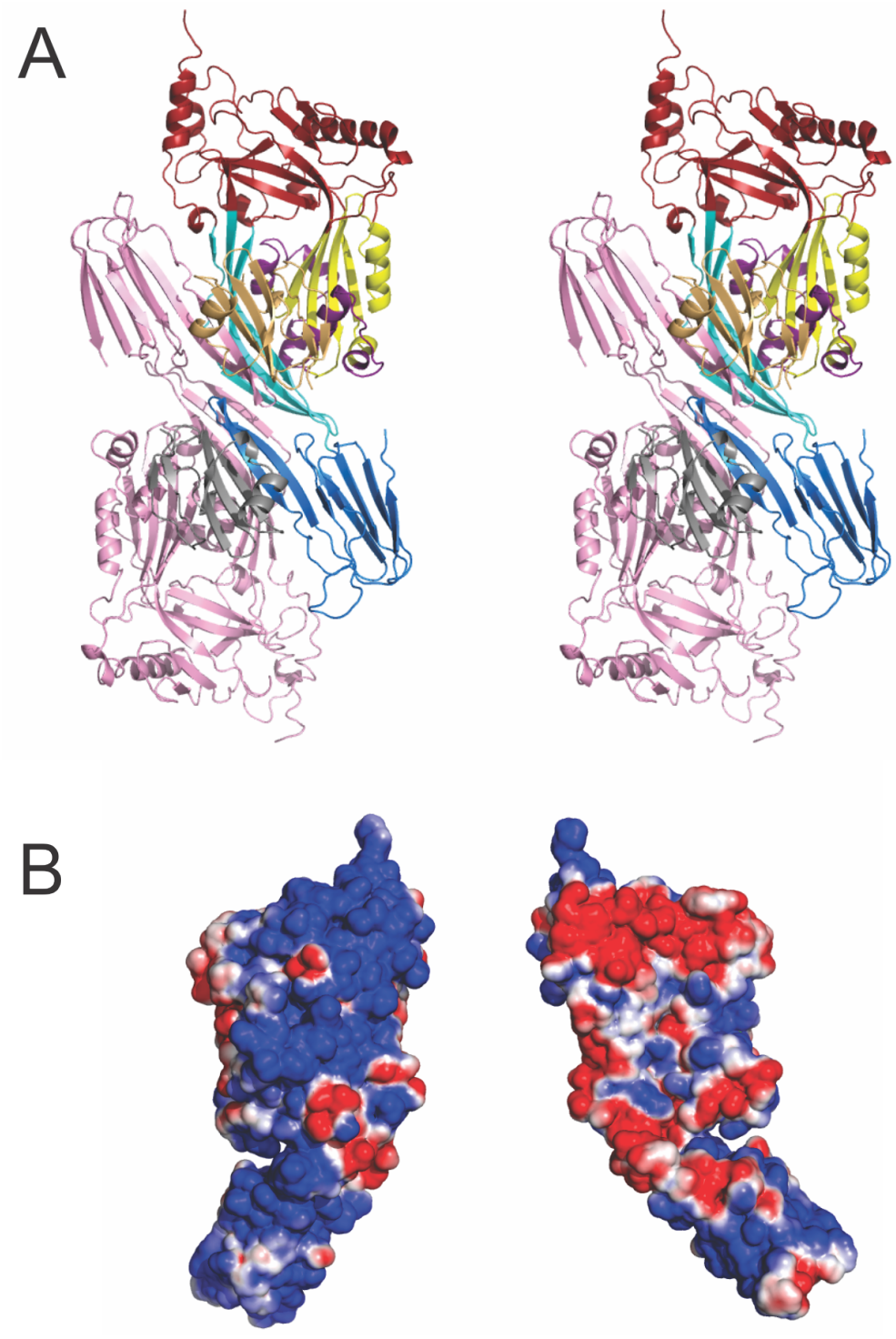

Figure S1. Representations of Key Features of the VLY-CD59 Structure. ***Related to Figure 1.***
(A) Stereo view of the VLY^{ml}-$CD59^{D22A}$ complex asymmetric unit showing the intertwined nature of the CDC "dimer". One VLY^{ml} monomer is colored by domain as in Figure 1, with its associated $CD59^{D22A}$ molecule in grey. The second VLY^{ml} monomer is colored pink with its $CD59^{D22A}$ in orange.
(B) Orthogonal views of the solvent accessible surface of VLY^{ml} colored by local electrostatics (red: -1kT/e to blue: +1Kt/e) showing the disparity in the charge on the two faces of the protein. Electrostatics were calculated using the APBS plugin (Baker et al., 2001) for PyMOL (Schrodinger, 2015).

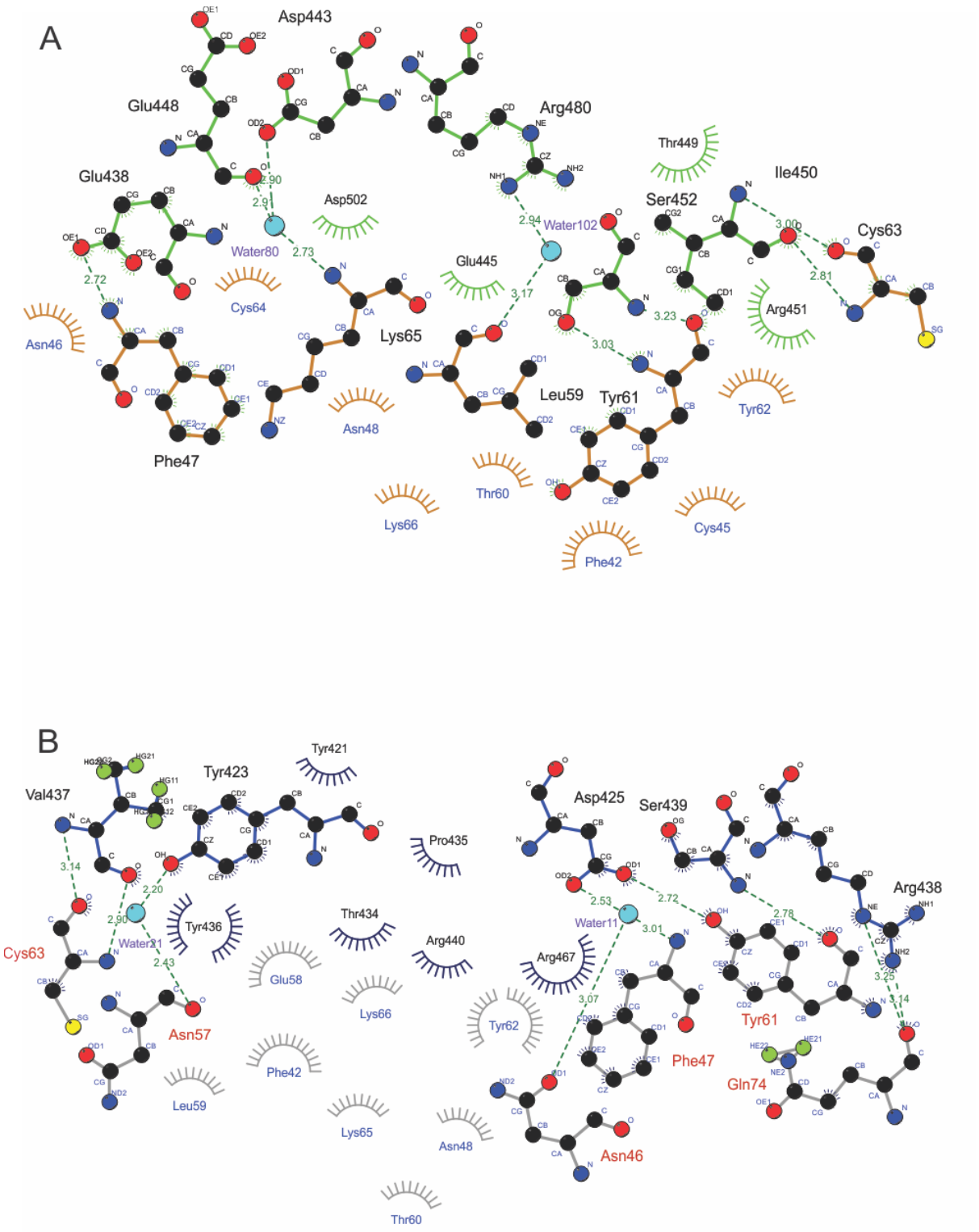

Figure S2. LIGPLOT (Wallace et al., 1995) Views of CDC-CD59 Interactions. ***Related to Figure 2.***
(A) ILY^{ml} (green bonds)-CD59^{D22A} (brown bonds) complex.
(B) VLY^{ml} (blue bonds)-CD59^{D22A} (grey bonds).

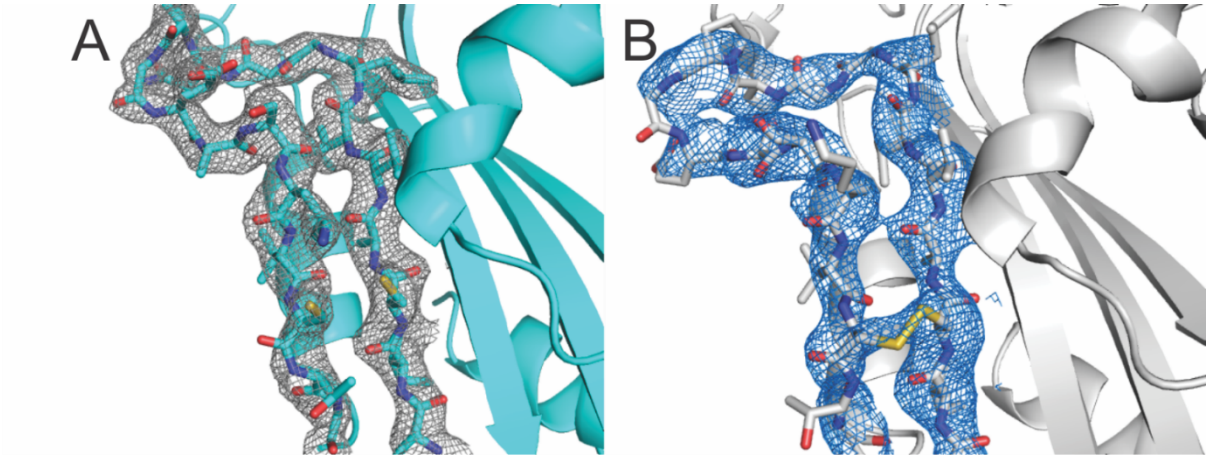

Figure S3. Electron Density Shots of the Engineered Disulfides in Domain 3. ***Related to Figure 1.***
Views of the final $2F_O$-F_C electron density map (contour level 1σ in blue or grey).
(A) ILY^{ml}-CD59^{D22A} complex.
(B) ILY^{ml}.

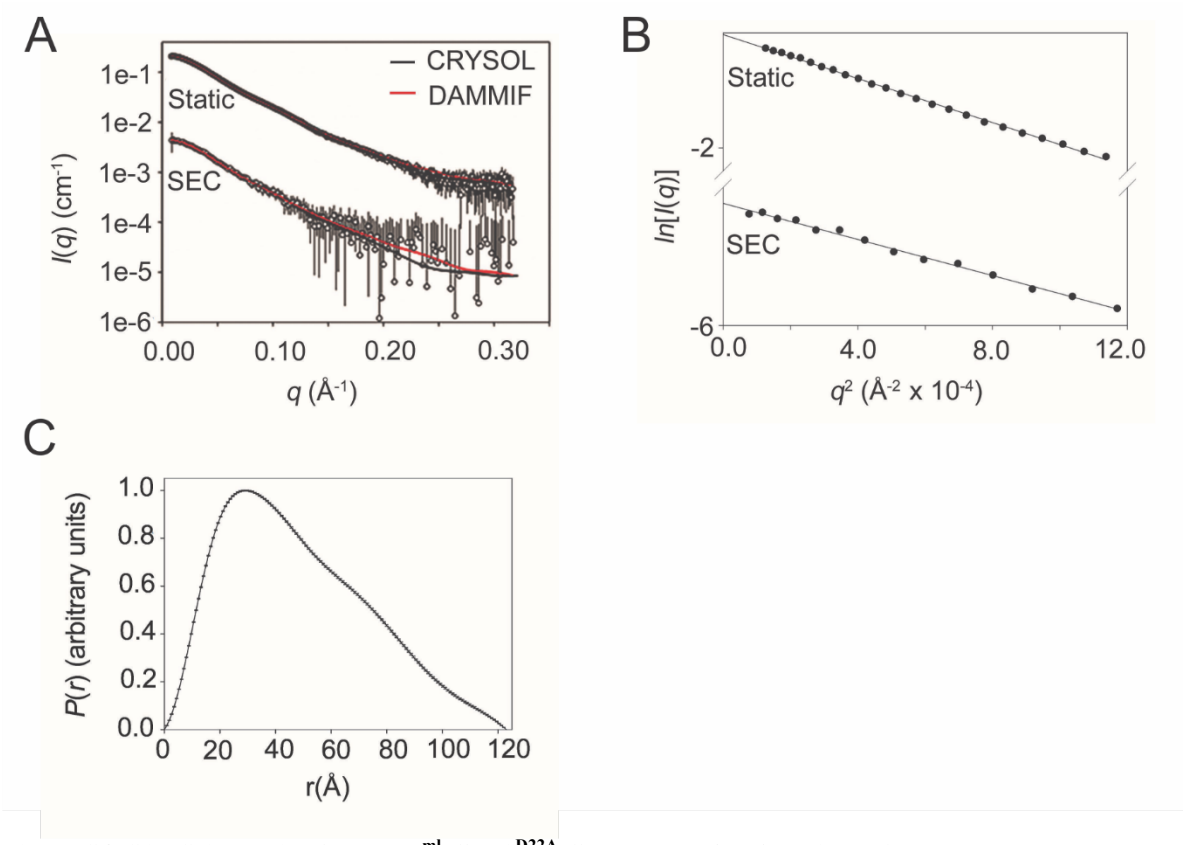

Figure S4. SAXS Analysis of the ILY^{ml}-CD59^{D22A} Complex. ***Related to Figure 3.***

(A) The mean intensities as a function of the magnitude of the scattering vector ($I(q)$ vs. q) are shown as circles and the error bars indicate ± 1 standard deviation. The upper data set is from a static sample at 5.6 mg/ml. The lower data set is for a SEC-SAXS sample at 0.12 mg/ml. For each data set, the theoretical scattering profile of the crystallographic model of the ILY^{ml}-CD59^{D22A} complex was fitted to the experimental data using CRYSOL (Svergun et al., 1995) and is shown as a solid black line (χ_{CRYSOL} = 0.845 and 0.309 for the static and SEC data sets, respectively). The fit of the theoretical scattering profile of a representative dummy atom model generated by DAMMIF (Franke and Svergun, 2009) is shown as a solid red line (χ_{DAMMIF} = 0.749 and 0.304 for the static and SEC data sets, respectively).

(B) Guinier plots. Data points satisfied $q.R_g$ <1.3 for both data sets are shown (R_g = 37.9 ± 0.2 Å and 37.4 ± 2.2 Å for the static and SEC data sets, respectively.

(C) The P(r) pair distance vector distribution function generated from the static SAXS data set using DATGNOM (Petoukhov et al., 2012).

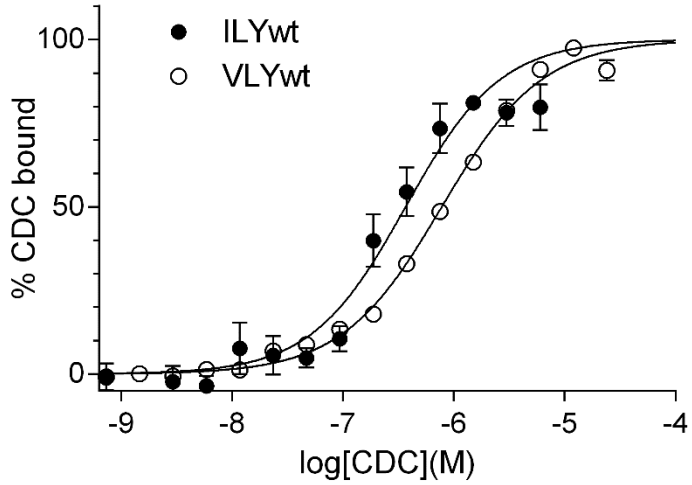

Figure S5. CD59^{D22A} Binding to Increasing Concentrations of ILY^{wt} and VLY^{wt} derived from MST data. ***Related to Figure 2.***

CD59^{D22A} binding to increasing concentrations of ILY^{wt} (closed circles) and VLY^{wt} (open circles). Data were normalised to percentage protein bound (ΔFnorm/amplitude x 100). The average K_D values were calculated from five independent ILY^{wt}/CD59^{D22A} replicates and four independent VLY^{wt}/CD59^{D22A} replicates. ILYwt binds CD59^{D22A} with a K_D of 367 ± 46 nM, two fold higher than the affinity of VLY^{wt} for CD59^{D22A} which has a K_D of 779 ± 30 nM ($p < 0.0001$). Solid lines represent fits of a sigmoidal function to the experimental data points.

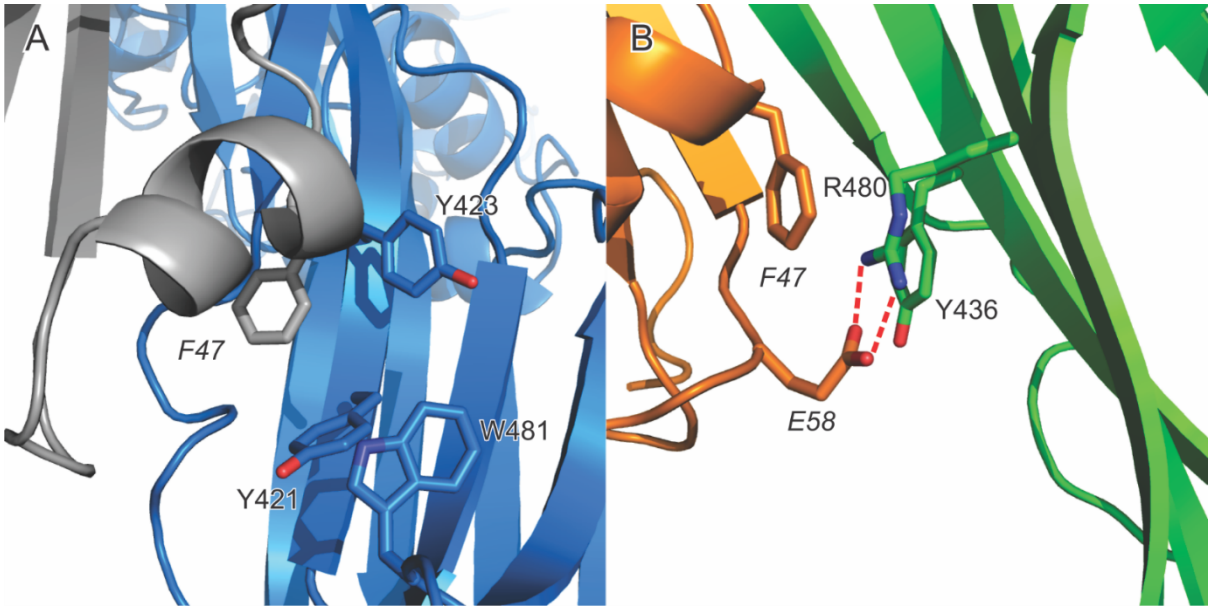

Figure S6. Comparison of the Key Interactions Associated with the Y-X-Y CD59-Binding Motif in Molecular Dynamics Simulations of VLY^{wt}-CD59 and ILY^{wt}-CD59 Complexes. ***Related to Figure 2.***

(A) In VLY^{wt} a stabilising aromatic box forms between the F47 side-chain of CD59 (grey) and the side-chains of Y423 (face-packed) and Y421 (edge-face packed) from VLY^{wt}. W481, the last tryptophan residue of the conserved undecapeptide motif is packed against Y421 in another edge-face interaction, further locking the aromatic box in to place.

(B) In ILY^{wt} R480 sits between the aromatic rings of F47 from CD59 and Y436 of ILY^{wt} and forms a salt bridge (red dashed lines) with E58 of CD59. The second tyrosine of the ILY^{wt} Y-X-Y motif, Y434 (not shown), does not appear to be involved in the interaction.

SUPPLEMENTAL TABLES

Table S1. SAXS data collection and scattering-derived parameters
Related to Figure 3 and main-text Experimental Procedures

Data-collection parameters		
Instrument	Australian Synchrotron SAXS/WAXS beamline	
Beam geometry	Point collimation (250 μm horizontal × 150 μm vertical)	
Wavelength (Å)	1.03320	
	In-line SEC	Static capillary
q range (Å^{-1})	0.0088-0.3232 (162 points)	0.0083-0.3169 (317 points)
Exposures	80 × 2 s	18 × 1 s
Concentration (mg/ml)	0.12	5.60
Temperature (K)	298	298
Structural parameters[a]		
$I(0)$ (cm^{-1}) [from $P(r)$]	0.0046 ± 0.0001	0.2223 ± 0.0005
R_g (Å) [from $P(r)$]	37.9 ± 1.1	38.9 ± 0.1
$I(0)$ (cm^{-1}) (from Guinier)	0.0046 ± 0.0002	0.2218 ± 0.0008
R_g (Å) (from Guinier)	37.4 ± 2.2	37.9 ± 0.2
D_{max} (Å) [b]	121 ± 5	123 ± 3
Porod volume estimate (Å^3)	102200	96176
Dry volume from sequence (Å^3)	82206	82206
Molecular mass determination		
From sequence (kDa)	67.9 (58.8 + 9.1)	67.9 (58.8 + 9.1)
From Porod volume (kDa) [c]	70.7	66.5

[a] Reported for the averaged SAXS data
[b] D_{max} is a model parameter and uncertainty is based on $P(r)$ analyses with a range of D_{max} values
[c] Calculated from the Porod volumes by direct comparison with a glucose isomerase standard.

SUPPLEMENTAL EXPERIMENTAL PROCEDURES
Related to main-text Experimental Procedures

Cloning, Expression and Purification

The *E. coli* codon optimized VLY gene construct, lacking the 31 residue N terminal signal sequence, pET28a/coVLY31, has been previously described (Gelber et al., 2008). VLY coding sequence A31 – D516 (VLY_{31}) was amplified by PCR and cloned into pMCSg7 by LIC cloning. The monomer locked form, VLY_{31}^{ml} containing mutations T333C and I348C was created using the QuikChange™ Site-Directed Mutagenesis Kit (Stratagene) according to the manufacturer's instructions. The monomer locked mutant of ILY (ILY^{ml}, T346 and I361 mutated to cysteines) has been previously described (LaChapelle et al., 2009).

His_6-$VLY_{31,}$ His_6-VLY_{31}^{ml}, His_6-ILY^{wt} and His_6-ILY^{ml} constructs were expressed in *E. coli* BL21 (DE3) pREP4 in Turbo Broth medium (Athena Enzyme systems, Baltimore) at 37°C. The cell pellet was resuspended at 21°C in lysis buffer (25 mM Tris, 500 mM NaCl, 10% (v/v) glycerol, 0.1% (v/v) Triton X-100, 100 µM PMSF, 10 µg/ml lysozyme, 10 µg/ml DNAse 1, 20 mM imidazole, pH 7.2). Cells were lysed by incubating at 21°C shaking for 1 hour, then sonicated 6 x 10 seconds. The His_6 constructs were purified on a 5 ml HisTrap ™ HP column (GE), equilibrated in Buffer A, pH 7.2 (25 mM Tris, 500 mM NaCl, 20 mM imidazole, 10% glycerol, pH 7.2). The column was washed with 50 ml Buffer A, pH 7.2. The proteins were eluted from the column with Buffer B (25 mM Tris, 500 mM NaCl, 400 mM imidazole, 10% glycerol, pH 7.2). Fractions containing the His_6 constructs were pooled and dialyzed into 20 mM HEPES, 300 mM Na_2SO_4, 10% (v/v) glycerol, pH 7.0 at 21°C for 16 hours. His tag cleavage of His_6-VLY_{31} and His_6-VLY_{31}^{ml} was carried out by adding TEV 1:50 molar ratio to His_6VLY and incubating at 21°C for 2 hours. His_6VLY/TEV was dialyzed into 20 mM Tris pH 7.2, 20 mM imidazole, 500 mM NaCl, 10% glycerol and loaded onto a 5 ml HisTrap column as before. VLY_{31} or VLY_{31}^{ml} protein without the His_6 tag ('VLY^{wt}' or 'VLY^{ml}') was collected in the flow through. VLY^{ml} or VLY^{wt} was dialyzed into 20 mM HEPES, 300 mM Na_2SO_4, 10% (v/v) glycerol, pH 7.0 and further purified by size exclusion chromatography (SEC) on a Superdex 200 26/60 column (GE) in the same buffer. Fractions containing monomeric VLY^{ml} or VLY^{wt} protein (monitored by SDS PAGE) were pooled and concentrated to 3.5 mg/ml and stored at -80°C.

Dialyzed His_6-ILY^{ml} was further purified by size exclusion chromatography (SEC) on a Superdex 200 26/60 column (GE) in 20 mM HEPES pH 7.0, 300 mM Na_2SO_4, 10% glycerol. Fractions containing monomeric His_6-ILY^{ml} protein (monitored by SDS PAGE) were pooled and concentrated to 6 mg/ml and stored at -80°C.

CD59

CD59 was amplified from an IMAGE:4776621 cDNA clone of huCD59 using oligos: 5' TACTTCCAATCCAATGCTCTGCAGTGCTACAACTGTCCT;3'TTATCCACTTCCAATTAATTTTCAAGC TGTTCGTTAAA and was cloned into vector pMCSG7. This encoded a His_6-TEV-CD59 fusion protein which after TEV cleavage of the hexahistidine tag yielded the CD59 coding region of the mature protein [L1-P103 with an N terminal additional serine, asparagine, alanine]. Point mutation D22A was introduced with oligos: 5' TGTTCATCTGCCTTTGATGCG3' and complement 5' CGCATCAAAGGCAGATGAACA 3' using the Quik Change Mutagenesis kit (Stratagene), according to manufacturer's instructions. His_6-TEV-$CD59^{D22A}$ was expressed in *E. coli* BL21 (DE3) pREP4 in Luria Broth (LB) medium at 37°C. The cell pellet was resuspended at 21°C in lysis buffer (50 mM Tris pH 8.0, 100 mM NaCl, 10 % (v/v) glycerol, 0.1% Triton X-100, 100 µM PMSF, 10 µg/ml lysozyme, 10 µg/ml DNAse 1. Cells were lysed by incubating at 21°C shaking for 1 hour, then sonicated 6 x 10 seconds. CD59 containing inclusion bodies were isolated by centrifugation at 20,000g for 20 minutes. Inclusion bodies were solubilized in Buffer A, pH 8.0 with 8 M urea (500 mM NaCl, 25 mM Tris, 20 mM imidazole, 8 M urea, pH 8.0). His_6-TEV-$CD59^{D22A}$ was purified on a 5 ml HisTrap ™ HP column (GE), equilibrated in Buffer A, pH 8.0 with 8 M urea. The column was washed with 50 ml Buffer A, pH 8.0 with 8 M urea. His_6-TEV-$CD59^{D22A}$ was eluted from the column with Buffer B (25 mM Tris, 500 mM NaCl, 400 mM imidazole, pH 8.0) with 8 M urea. Fractions containing His_6-TEV-$CD59^{D22A}$ were pooled and refolded as described by Leath *et al.* (2007). After refolding, His_6-TEV-$CD59^{D22A}$ was concentrated and dialyzed into 20 mM Tris pH 7.2 and 150 mM NaCl and incubated with a 1:50 molar ratio of His_6-TEV-$CD59^{D22A}$ to TEV to remove the hexahistidine tag. The protein solution was dialyzed into 20 mM Tris, 500 mM NaCl, 20 mM imidazole, pH 8.0 and purified on a 5 ml HisTrap ™ HP column (GE), equilibrated in Buffer A, pH 8.0, to remove the His tag and His-TEV. The purified $CD59^{D22A}$ passed through the column and was dialyzed into 20 mM HEPES, pH 7.0, 150 mM NaCl, at 4°C for 16 hours. Dialyzed $CD59^{D22A}$ was further purified by SEC on a Superdex 75 26/60 column in 20 mM HEPES, pH 7.2, 150 mM NaCl. Fractions containing monomeric $CD59^{D22A}$ protein (as monitored by SDS PAGE) were pooled and concentrated to 10 mg/ml and stored at -80°C.

CDC-CD59 Complex Formation

Either VLY^{ml} or His$_6$-ILY^{ml} were mixed with monomeric CD59^{D22A} in a 1:3 molar ratio and dialyzed into 20 mM HEPES, pH 7.0, 150 mM NaCl, at 21°C for 2 hours. The dialyzed complex was purified by SEC on a GE Superdex 200 26/60 column in 20 mM HEPES pH 7.0 and 150 mM NaCl. Fractions containing the VLY^{ml}-CD59^{D22A} complex or the ILY^{ml}-CD59^{D22A} complex were pooled and concentrated to 3.5 mg/ml and 6 mg/ml respectively, and stored at -80°C. Complex formation was verified by comparative SEC of monomer locked CDC and CDC-CD59 complex and SDS-PAGE of complex peak fractions.

Crystallizations

VLY^{ml}-CD59^{D22A} Complex

Initial crystallization trials of the VLY^{ml}-CD59^{D22A} complex were set up at 21 ºC on a Crystal Gryphon robot (ARI, Sunnywale CA, USA) in 96 well sitting drop format using Rigaku UV+ 96 plates (AXT, Sydney, Australia). Drops containing 0.2 µl of protein and 0.2 µl of crystallization solution were equilibrated against 35 µl of crystallization solution. Sparse matrix crystallization screens were conducted using MCSG+ screens 1 to 4 (Microlytic, USA) with the VLY^{ml}-CD59^{D22A} complex at a concentration of 3.9 mg/ml in 20 mM HEPES pH 7.2, 150 mM NaCl. Crystals initially formed in MCSG+ screen 1, condition 25 (0.1 M ammonium acetate, 17% PEG 10 K, 0.1 M Bis-Tris pH 5.5) at 21°C. Optimization of crystallization conditions were performed using the hanging drop vapor diffusion method in Linbro culture plates (ICN, Biochemicals Inc., Ohio, USA) at 21°C. Drops of 1 µl VLY^{ml}-CD59^{D22A} (2.65 mg/ml) mixed with an equal volume of precipitant were hung over 0.5 ml of well solution consisting of 0.1 M ammonium acetate, 17% PEG 10 K and 0.1 M Bis-Tris pH 5.5. 10 mM $MgCl_2$ was added to the drop only. Cryoprotection was achieved by the addition of 20% v/v PEG 400 to the drop and incubation at 21°C for 30 minutes before freezing in liquid nitrogen.

ILY^{ml}

Crystallization of ILY^{ml} was performed using the same protocol as previously reported for ILY^{wt} (Polekhina et al., 2004). Crystals were cryo-protected by transferring to a drop of 100mM MES pH 6.5, 75 mM NaCl, 18% PEG 8000 and directly adding 5% v/v MPD to the drop, every 30 minutes to a final concentration of 20% v/v MPD.

ILY^{ml}-CD59^{D22A} Complex

Initial crystallization trials were set up at 21 ºC on a Crystal Gryphon robot (ARI, Sunnywale CA, USA) in 96 well sitting drop format using Rigaku UV+ 96 plates (AXT, Sydney, Australia). Drops containing 0.2 µl of protein and 0.2 µl of crystallization solution were equilibrated against 35 µl of crystallization solution. Sparse matrix crystallization screens were conducted using MCSG+ screens 1 to 4 (Microlytic, USA) with the ILY^{ml}CD59^{D22A} complex at a concentration of 6 mg/ml. Crystals initially formed in MCSG+ screen 3, number 36 (10 % w/v PEG 8000, 0.2 M zinc acetate and 0.1 M MES, pH 6.0). Optimization of crystallization conditions was performed using the hanging drop vapor diffusion method at 21°C. 1 µl of ILY^{ml}-CD59^{D22A} was mixed with an equal volume of precipitant and hung over 0.5 ml of well solution of 10% w/v PEG 8000, 0.2 M zinc acetate, 100 mM MES pH 6.0 and 1 mM copper sulfate. Prior to freezing the crystals were cryo-protected by adding 4 times 0.2 µl of 10 M LiCl into the drops. The time interval between the additions was approximately 30 minutes.

Data Collection, Structure Determination and Refinement

Data were collected at the MX2 beamline at the Australian Synchrotron (Clayton, Victoria). Data collection was controlled using Blue-Ice software (McPhillips et al., 2002).

VLY^{ml}-CD59^{D22A}

The collected data were processed using the program XDS (Kabsch, 2010). Data from three separate crystals were merged to produce the final dataset. The space group was $P2_12_12$ with unit cell dimensions of a = 81.4 Å, b = 141.1 Å, c = 106.8 Å. The asymmetric unit contained two copies of the VLY^{ml}-CD59^{D22A} complex, with a solvent content of approximately 53% according to Matthews' coefficient calculations (Matthews, 1968). Molecular replacement was performed using the program PHASER (McCoy et al., 2007) in the PHENIX program suite (Adams et al., 2002). The search model was a low resolution (~4 Å) unpublished structure of VLY-CD59 determined from a different crystal form in-house (data not shown). The two CD59 molecules (PDB code: 2J8B, (Leath et al., 2007)) were located during another round of molecular replacement keeping the VLY structures fixed. Model building was performed with the program COOT (Emsley and Cowtan, 2004) and the programs REFMAC 5 (Murshudov et al., 1997) and PHENIX (Adams et al., 2002) were used for refinement. Individual B-factors were refined without the use of NCS constraints and bulk solvent and anisotropic scaling were applied. The final model yielded an R_{factor} and R_{free} of 23.4% and 27.3%, respectively. All residues of both proteins were visible in the electron density map except residues at the N-terminal ends of both VLY^{ml} chains, which were not built as the electron density was not well defined. In addition to the protein

components, the final model of the complex includes 137 water molecules. The geometry of the model was good with a Ramachandran plot showing 97.4% of the residues in the allowed regions. Data and refinement statistics are listed in Table 1.

ILY^{ml}

Data processing was performed using the program XDS (Kabsch, 1993). The space group was $P2_12_12$ with unit cell dimensions of a = 84.5 Å, b = 101.6 Å, c = 175.7 Å. These unit cell dimensions were similar to ILY^{wt}. The program POINTLESS (CCP4 program suite) detected the presence of pseudotranslational symmetry. During molecular replacement calculations this pseudotranslational symmetry was corrected using PHASER (McCoy et al., 2007) which is part of the PHENIX program suite (Adams et al., 2002). A solution was found with a monomer of ILYwt (PDB code: 1S3R; (Polekhina et al., 2005)) as a search model. Model building was performed with the program COOT (Emsley and Cowtan, 2004). Bulk solvent, anisotropic scaling and NCS restraints were applied and individual B-factor and TLS parameters were refined. The model yielded a final R_{factor} and R_{free} of 21.5% and 27.6%, respectively. ILY^{ml} molecule A superimposes onto molecule B with rmsd of 0.5 Å. Due to ambiguous electron density for residues 326 to 341 of monomer A and residues 326 to 340 in monomer B had to be removed. These residues were part of the TMH2 region. Additionally, due to lack of electron density residues 487 to 493 belonging to the trp-rich loop were deleted in monomer A. L1 to L3 loops in domain 4 had patches of bad electron density but the residues were not deleted. The mutation of residues T346 and I361 of ILY^{ml} into cysteines could be confirmed but the expected disulfide bridge between these residues could only be seen in monomer B. Monomer A exhibited poor density in the vicinity of this mutation. Due to the low resolution water molecules could not the placed in the electron density map. Stereochemical analysis of the refined structure using the program PROCHECK (Laskowski et al., 1993) gave a value of 99.2% in the allowed regions of the Ramachandran plot. There were 6 outliers (S358 (molecules A and B); I365 (molecules A an B); A319 (molecule B) and L496 (molecule B)) in the structure all located in regions of insufficient electron density. The statistics for data processing and refinement are presented in Table 1.

ILY^{ml}-CD59^{D22A} Complex

The collected data were processed using the program iMOSFLM (Battye et al., 2011) and SCALA (Winn et al., 2011). The space group was $C222_1$ with unit cell dimensions of a = 93.7 Å, b = 166.6 Å, c = 118.3 Å. The asymmetric unit contained one molecule with a solvent content of approximately 68% according to Matthews' coefficient calculations (Matthews, 1968). Molecular replacement was performed using the program PHASER (McCoy et al., 2007) in the CCP4 program suite (Winn et al., 2011). The search model was the structure of domain 1to domain 3 of ILY (PDB code: 1S3R; (Polekhina et al., 2005)) as domain 4 can adopt different orientations in CDCs (Bourdeau et al., 2009; Polekhina et al., 2005; Rossjohn et al., 1997; Xu et al., 2010). Subsequently domain 4 was found by fixing the solution obtained for domain 1 to domain 3. The CD59 (PDB code: 4BIK, (Johnson et al., 2013)) was located during another round of molecular replacement. Model building was performed with the program COOT (Emsley and Cowtan, 2004) and the programs REFMAC 5 (Murshudov et al., 1997) and PHENIX (Adams et al., 2002) were used for refinement. Individual B-factor and TLS parameters were refined and bulk solvent and anisotropic scaling was applied. The final model yielded an R_{factor} and R_{free} of 20.2 % and 25.9 %, respectively. All residues of both proteins were visible in the electron density map except residues 327 to 338 of ILY^{ml}, located in TMH2, which were not built as the electron density was not well defined. In addition to the protein components, the final model of the complex includes 127 water molecules and 2 SO_4^{2-} ions, one bound to Q255 and one to H242, and 7 Zn^{2+} ions. The geometry of the model was good with a Ramachandran plot showing 100% of the residues in the allowed regions. Data and refinement statistics are listed in Table 1.

Small Angle X-ray Scattering

SAXS data were collected on the SAXS/WAXS beamline at the Australian Synchrotron (Clayton, Victoria) (Table S1) (Kirby et al., 2013). The X-ray beam size was 250 µm horizontal x 120 µm vertical. Data collection was on a Dectris-Pilatus 200K detector. Sample to detector distance was 2676.22 mm (q-range 0.06 - 0.35 Å^{-1}) with a 12 Ke V beam and X-ray wavelength of 1.0322 Å. SAXS data from samples of the ILY-CD59 complex were recorded in static mode and using in-line gel filtration (SEC-SAXS) (Gunn et al., 2011). In static mode, SEC purified, ILY^{ml}-CD59^{D22A} complex solution (48 µl at 6 mg/ml in 20 mM HEPES pH 7.2, 150 mM NaCl) was automatically sampled from a 96 well plate. Data acquisition was at 298 K with 2 second exposures (2.1 sec. repeat time). In SEC-SAXS mode, samples (48 µl at 6 mg/ml in 20 mM HEPES pH 7.2, 150 mM NaCl) were run with a Wyatt Technology WTC-050N5G SEC column equilibrated in the same buffer. The column flow rate was 0.5 ml min^{-1} at 298 K and exposures were 2 seconds (2.1 sec. repeat time). Data acquisition and reduction analysis were carried out with Australian Synchrotron scatterBrain 9-1_0 software (Kirby et al., 2013). Further analysis was carried out using ATSAS 2.6.0 data analysis software (Petoukhov et al., 2012). *Ab initio* shape reconstructions were performed using *DAMMIF* (Franke and Svergun, 2009). Shape envelope

cluster analysis was performed using DAMCLUST and averaged filtered shape envelopes were generated with *DAMAVER* (Volkov and Svergun, 2003). Theoretical scattering profiles were generated from model coordinates and compared to experimental data using *CRYSOL* (Svergun et al., 1995). Dry volume was calculated using http://www.basic.northwestern.edu/biotools/proteincalc.html. Statistical analysis of the goodness of fit of theoretical scattering profiles to experimental SAXS data and comparisons of the fits of SAXS data were performed as in Mills *et al.* (Mills et al., 2009).

Microscale Thermophoresis

MST solution binding studies between ILY^{wt} and $CD59^{D22A}$ and VLY^{wt} and $CD59^{D22A}$ were performed using standard protocols on a Monolith NT.115 (Nanotemper Technologies). $CD59^{D22A}$ was labeled with Dylight 650 Antibody labeling kit (Thermo Scientific™) according to the manufacturer's instructions. ILY^{wt} and VLY^{wt}were diluted in a two-fold dilution series from 48 μM to 0.14 nM in 20 mM HEPES pH 7.2, 150 mM NaCl, 0.05 mg/ml BSA and 0.1 % Tween 20. Each dilution was mixed 1:1 v/v with 10 μl 40 nM Dylight 650 labeled $CD59^{D22A}$. Final reaction concentrations were 0.07 nM - 24 μM for ILY^{wt} and VLY^{wt} and 20 nM labeled $CD59^{D22A}$. Assays were conducted in NanoTemper standard capillaries at 90% Red LED power, 40% laser power, heated for 30 sec, followed by 5 sec cooling. All experiments were performed with a minimum of 4 independent replicates. Data points 12 μM and 24 μM for ILY^{wt} were not included in the data analysis as these samples precipitated during assay. Affinity, K_D, was quantified by analyzing the change in normalized fluorescence (Fnorm = fluorescence after thermophoresis / initial fluorescence) as a function of the concentration of the titrated protein. The percentage of ILY^{wt} or VLY^{wt} bound (ΔFnorm/amplitude x 100) was plotted against the concentration of protein and the experimental data points were fit with a sigmoidal function using GraphPad Prism (Version 6, GraphPad, San Diego, CA, USA) and statistical significance was assessed using an extra-sum-of-squares F test. Data are expressed as means and SEM.

Molecular Modeling

The ILY-CD59 and VLY-CD59 systems were solvated with 70,872 water molecules and 0.15 M NaCl ions added to electrostatic neutrality using VMD (Humphrey et al., 1996). The approximate final dimensions of the systems were 121 Å x 142 Å x 214 Å. All simulations were conducted with NAMD 2.10 (Phillips et al., 2005) performed on either BlueGene/Q or Cray XC40 architecture. The systems were equilibrated using an NPT ensemble at 310 K at 1.01325 Bar for 5 nanoseconds. Long-range Coulomb forces were computed with the Particle Mesh Ewald method with a grid spacing of 1 Å. 2 fs timesteps were used with non-bonded interactions calculated every 2 fs and full electrostatics every 4 fs while hydrogens were constrained with the SHAKE algorithm. The cut-off distance was 12 Å with a switching distance of 10 Å and a pair-list distance of 14 Å. Pressure was controlled to 1 atmosphere using the Nosé-Hoover Langevin piston method employing a piston period of 100 fs and a piston decay of 50 fs. Trajectory frames were captured every 100 picoseconds. Five replicate production runs of the ILY model were run for 100 nanoseconds. The ILY-CD59 model was based on the published structure (PDB id: 4BIK) while the VLY structure was based on the one described here.

SUPPLEMENTAL ANALYSIS

Related to Figures 1 to 3

VLY^{ml}-$CD59^{D22A}$ Crystallographic Dimer

Despite extensive efforts we could not generate a stable complex with wild-type VLY suitable for structural studies. It is possible receptor engagement may have induced conformational changes associated with the formation of membrane-bound oligomers. However, a "monomer-locked" version of VLY, with an engineered disulfide that minimizes monomer-monomer interactions in the soluble form, did give a stable complex with CD59. The mutant design was based on a similar ILY mutant (LaChapelle et al., 2009) which prevents the disengagement of strand β5 from β4 in D3 a key step associated with the formation of membrane-bound oligomers. VLY^{wt} residues Thr 333 and Ile 348 were mutated to cysteines to generate the disulfide bridge between β-strands 4 and 5 in D3. For the structural studies we used a modified CD59 (D22A) as this protein has been shown previously to bind with higher affinity to ILY (Wickham et al., 2011). Two molecules of the complex were identified in the asymmetric unit of the crystal lattice and they adopt very similar structures (Figure S1). The VLY^{ml}-$CD59^{D22A}$ complex forms a head-to-tail dimer in the asymmetric unit of the crystal with extensive interactions between the two VLY^{ml} monomers, primarily through D2 but also involving residues in D4 (Figure S1). Comparison of the VLY^{ml} monomers present in the asymmetric unit shows that they are similar, with the main difference a reorientation and restructuring of D4. Superposition of each domain of molecule B on to molecule A with LSQMAN (Kleywegt and Jones, 1997) gives Cα RMSD values of D1: 1.1 Å, D2: 0.9 Å, D3: 1.3 Å and D4: 1.6 Å, with the whole protein having an RMSD of 1.9 Å or 1.5 Å for D1-3 alone. The introduced disulfide between residues 333 and 348 is clearly visible in both VLY^{ml} molecules and results in a stretch of protein with poor definition in the experimental electron density between G339 and K346, apparently due to

disruption of the β–sheet structure normally found in this part of D3. Packing between the two VLY^{ml} chains in the asymmetric unit is extensive with a buried surface area of approximately 1,000 $Å^2$ split fairly evenly between the two chains (500 and 445 $Å^2$ for chains A and B respectively). The shape complementarity (Sc) (Lawrence and Colman, 1993; Winn et al., 2011) of the interface, 0.69, indicates tight packing, being the same order as the Sc values seen for antibody-antigen complexes of ~0.65. The interface is formed partly as a continuation of the antiparallel β–sheet that makes up D2, with the first strand of D2 from each monomer packing against each other to create what appears to be a 6-stranded continuous sheet (Figure S1). The interface, however, is distorted and lacking in the classical network of backbone hydrogen bonds that are usually seen in β–sheet structures, with only a few symmetrical backbone (SerA79NH to SerB79O, SerA79O to SerB79NH) and side-chain to backbone (SerA81γO to PheB77NH, SerB81γO to PheA77NH) hydrogen bonds present. The other major interaction occurs where the loop at the end of the β–hairpin of D4 (residues T429 to G433) in each VLY^{ml} chain inserts into the pocket formed between the equivalent loops residues and parts of D2 and D3 (residues V90, V91, E92, T302, K399, V400 and S401) on the other chain (Figure S1).

Due to the arrangement of the crystallographic dimer, each $CD59^{D22A}$ also makes substantial contacts with D3 of the adjacent VLY^{ml} (Figure S1, S2). The $CD59^{D22A}$ from one complex packs against D2 and D3 of VLY^{ml} in the second complex. Specific interactions are limited between the proteins, with a single hydrogen bond between E76 of CD59 and T99 of VLY^{ml}. Only slightly less surface is buried in the interface (~620 $Å^2$, 320 $Å^2$ from VLY^{ml} and 300 $Å^2$ from $CD59^{D22A}$) than for the primary binding site, with a Sc value of 0.64. Although the Sc value is within the range of observed protein-protein interfaces (Lawrence and Colman, 1993), the size of the interface and lack of specific interactions support the interpretation that the interaction is an artifact of the crystal lattice. This secondary site is not the same as the secondary site described in the published ILY^{ml}-CD59 structure (Johnson et al., 2013).

The $CD59^{D22A}$ component of the complex adopts an almost identical structure to the published structures of the uncomplexed protein (PDB id: 2J8B; (Leath et al., 2007)) with a root-mean-square deviations (rmsd) of 0.4 Å and 0.3 Å over backbone alpha carbon atoms for the two $CD59^{D22A}$ molecules in the asymmetric unit of the VLY^{ml}-$CD59^{D22A}$ complex crystal structure. At the site of the D22A substitution the protein structure appears unchanged, with the altered residue on the distal side of $CD59^{D22A}$ with respect to the VLY^{ml} interface (Figure 2A). The two $CD59^{D22A}$ molecules in the asymmetric unit adopt very similar structures. The largest differences are in the turn between β–strands 3 and 4, encompassing residues 31 to 33, and at the very C-terminus of the protein for chain D in the complex. The shift in position of residues 31 to 33 appears unrelated to contacts with VLY^{ml} or to crystal contacts. The C-terminal residue, however, is in contact with VLY^{ml} in the VLY^{ml}-$CD59^{D22A}$ complex and within the crystallographic dimer, causing it to shift relative to the free CD59 structure as discussed in the main text.

Crystal Structure of ILY^{ml} – the Engineered Disulfide Bridge

Both ILY^{ml} monomers clearly show the presence of the disulfide (Figure S3B). The introduced disulfide bond causes a significant alteration of the short region from residue G352 to residue G363 as the pair of residues originally selected for site-directed mutagenesis (T346 and I361) are incorrectly oriented in the ILY^{wt} structure for simple pairing. The two residues are in adjacent strands of the D3 beta-sheet, but on opposite faces, such that the introduction of the disulfide bond at this point causes a 180º twist and a one residue shift in register in the β-5 strand.

Crystal Structure of ILY^{ml} Complexed to $CD59^{D22A}$ – the Engineered Disulfide Bridge

The electron density maps clearly supported the presence of both mutations but surprisingly there was no evidence of a disulfide bridge formed between them (Figure S3A), in contrast to the published low resolution structure (PDB id: 4BIK) (Johnson et al., 2013), which also made use of the ILY^{ml} protein and contains density consistent with an intact disulfide in both ILY^{ml} monomers. The electron density for uncomplexed ILY^{ml} shows the presence of the disulfide as well (Figure S3B). A possible explanation is that the disulfide bridge in ILY^{ml} in the complex crystals was broken during acquisition of our data by the high energy of the synchrotron beam (Burmeister, 2000). Nevertheless, in the $CD59^{D22A}$ molecule the expected five disulfide bridges were all present. Notably the local conformation of Gly352 to Gly363 in the ILY^{ml} protein in the complex remains in the twisted pose seen for ILY^{ml} alone.

Crystal Structure of ILY^{ml} Complexed to $CD59^{D22A}$ – the CD59 Mutations

Surprisingly, mutation of CD59 residue D22 to alanine caused a twofold increase in affinity for ILY (Wickham et al., 2011). As with the VLY^{ml}-$CD59^{D22A}$ complex, the structure of $CD59^{D22A}$ bound to ILY^{ml} is effectively identical to the free CD59 structure (PDB id: 2J88), with a 0.8 Å alpha carbon rmsd. D22 and F23 are located in a loop distant from ILY binding site that appears structurally unchanged from the free CD59 structure (Figure 2). How the D22A mutation causes increased binding is unclear, whereas the F23A mutation can be expected to

destabilize the protein as the F23 aromatic ring stabilizes the position of the loop in CD59 from C19 to D24 by packing against the C19-C39 disulfide bond.

Solution Structure of ILY^{ml}-CD59^{D22A}

The solution structure of the ILY^{ml}-CD59^{D22A} complex was initially analyzed by SAXS in combination with size exclusion chromatography (SEC-SAXS) (Gunn et al., 2011). The scattering species eluted in a single elution peak and Guinier analysis of these data gave a radius of gyration (R_g) of 37.4 ± 2.2 Å (Table S1 and Figure S4B). However, due to dilution on the column these SEC-SAXS data had a very low signal to noise and were unsuitable for shape modelling and detailed analysis. Additional SAXS data were recorded from the undiluted complex (5.6 mg/ml) in static sample mode. The R_g (37.9 ± 0.2 Å) and the other invariant structural parameters obtained from the static sample were in good agreement with those from the SEC sample (Table S1), indicating that concentration-dependent aggregation was not an issue and all further analyses were conducted using the static SAXS data. The molecular mass of the scattering species was calculated to be 66.5 kDa using the volume estimates provided by Porod analysis of the SAXS data from the static sample and a glucose isomerase standard (172 kDa). This is in good agreement with the theoretic molecular mass of a 1:1 complex of 67.9 kDa (58.8 + 9.1 kDa, for His_6ILY^{ml} + $CD59^{D22A}$). The shape of the $P(r)$ curve generated from the static SAXS data is consistent with an elongated multi-domain structure (Figure S4C). *Ab initio* shape envelope reconstructions were performed using dummy atom modeling in DAMMIF (Franke and Svergun, 2009). Significant shape heterogeneity was observed in the first 10 envelopes calculated, so a total of 30 envelopes were calculated and subjected to cluster analysis using DAMCLUST. The most highly populated cluster contained 8 envelopes with mean normalized spatial discrepancy (NSD) of 0.899 ± 0.048. The average, filtered shape envelope from this most highly populated cluster overlays well with our crystallographic model of the ILY-CD59 complex (Figure 3). Indeed, this cluster is more similar in shape to the crystallographic model, compared to the remaining envelopes (median NSD of 1.16, n=8; *c.f.* median NSD = 1.29 (n=22); p=0.033, Wilcoxon-Mann-Whitney test, 1-tailed). The theoretical scattering profile generated from the coordinates of the ILY^{ml}-CD59^{D22A} crystallographic model was fitted to the static SAXS using CRYSOL (Svergun et al., 1995) (Figure S4A). The fit to the static SAXS data was very good (χ_{CRYSOL} = 0.845; $P_\chi(\chi^2;\nu)$ >0.999) (statistical analysis as per Mills et al., 2009). The fit of all alternate crystallographic 1:1 and 1:2 ILY-CD59 models, from the previously published ILY-CD59 structure (PDB id: 4BIK) (Johnson et al., 2013), were significantly worse (χ_{CRYSOL} >1.182; $P_F(F;\nu_1,\nu_2)$ <1.2e-9).

SUPPLEMENTAL REFERENCES

Adams, P.D., Grosse-Kunstleve, R.W., Hung, L.W., Ioerger, T.R., McCoy, A.J., Moriarty, N.W., Read, R.J., Sacchettini, J.C., Sauter, N.K., and Terwilliger, T.C. (2002). PHENIX: building new software for automated crystallographic structure determination. Acta Crystallogr D Biol Crystallogr *58*, 1948-1954.

Baker, N.A., Sept, D., Joseph, S., Holst, M.J., and McCammon, J.A. (2001). Electrostatics of nanosystems: application to microtubules and the ribosome. Proc Natl Acad Sci U S A *98*, 10037-10041.

Battye, T.G., Kontogiannis, L., Johnson, O., Powell, H.R., and Leslie, A.G. (2011). iMOSFLM: a new graphical interface for diffraction-image processing with MOSFLM. Acta Crystallogr D Biol Crystallogr *67*, 271-281.

Bourdeau, R.W., Malito, E., Chenal, A., Bishop, B.L., Musch, M.W., Villereal, M.L., Chang, E.B., Mosser, E.M., Rest, R.F., and Tang, W.J. (2009). Cellular functions and X-ray structure of anthrolysin O, a cholesterol-dependent cytolysin secreted by Bacillus anthracis. J Biol Chem *284*, 14645-14656.

Burmeister, W.P. (2000). Structural changes in a cryo-cooled protein crystal owing to radiation damage. Acta Crystallogr D Biol Crystallogr *56*, 328-341.

Emsley, P., and Cowtan, K. (2004). Coot: model-building tools for molecular graphics. Acta Crystallogr D Biol Crystallogr *60*, 2126-2132.

Franke, D., and Svergun, D.I. (2009). DAMMIF, a program for rapid ab-initio shape determination in small-angle scattering. Journal of applied crystallography *42*, 342-346.

Gunn, N.J., Gorman, M.A., Dobson, R.C., Parker, M.W., and Mulhern, T.D. (2011). Purification, crystallization, small-angle X-ray scattering and preliminary X-ray diffraction analysis of the SH2 domain of the Csk-homologous kinase. Acta Crystallogr Sect F Struct Biol Cryst Commun *67*, 336-339.

Humphrey, W., Dalke, A., and Schulten, K. (1996). VMD: visual molecular dynamics. J Mol Graph *14*, 33-38, 27-38.

Kleywegt, G.J., and Jones, T.A. (1997). Detecting folding motifs and similarities in protein structures. Methods Enzymol *277*, 525-545.

Laskowski, R.A., MacArthur, M.W., Moss, D.S., and Thornton, J.M. (1993). PROCHECK: a program to check the stereochemical quality of protein structures. Journal of applied crystallography *26*, 283-291.

Leath, K.J., Johnson, S., Roversi, P., Hughes, T.R., Smith, R.A., Mackenzie, L., Morgan, B.P., and Lea, S.M. (2007). High-resolution structures of bacterially expressed soluble human CD59. Acta Crystallogr Sect F Struct Biol Cryst Commun *63*, 648-652.

Matthews, B.W. (1968). Solvent content of protein crystals. J Mol Biol *33*, 491-497.

McPhillips, T.M., McPhillips, S.E., Chiu, H.J., Cohen, A.E., Deacon, A.M., Ellis, P.J., Garman, E., Gonzalez, A., Sauter, N.K., Phizackerley, R.P*., et al.* (2002). Blu-Ice and the Distributed Control System: software for data acquisition and instrument control at macromolecular crystallography beamlines. Journal of synchrotron radiation *9*, 401-406.

Murshudov, G.N., Vagin, A.A., and Dodson, E.J. (1997). Refinement of macromolecular structures by the maximum-likelihood method. Acta Crystallogr D Biol Crystallogr *53*, 240-255.

Petoukhov, M.V., Franke, D., Shkumatov, A.V., Tria, G., Kikhney, A.G., Gajda, M., Gorba, C., Mertens, H.D., Konarev, P.V., and Svergun, D.I. (2012). New developments in the program package for small-angle scattering data analysis. Journal of applied crystallography *45*, 342-350.

Polekhina, G., Giddings, K.S., Tweten, R.K., and Parker, M.W. (2004). Crystallization and preliminary X-ray analysis of the human-specific toxin intermedilysin. Acta Crystallogr D Biol Crystallogr *60*, 347-349.

Schrodinger, LLC (2015). The PyMOL Molecular Graphics System, Version 1.8.

Svergun, D., Barberato, C., and Koch, M.H.J. (1995). CRYSOL - a Program to Evaluate X-ray Solution Scattering of Biological Macromolecules from Atomic Coordinates. Journal of applied crystallography *28*, 768-773.

Wallace, A.C., Laskowski, R.A., and Thornton, J.M. (1995). LIGPLOT: a program to generate schematic diagrams of protein-ligand interactions. Protein Eng *8*, 127-134.

Xu, L., Huang, B., Du, H., Zhang, X.C., Xu, J., Li, X., and Rao, Z. (2010). Crystal structure of cytotoxin protein suilysin from Streptococcus suis. Protein Cell *1*, 96-105.